Engineering Fracture Mechanics 306 (2024) 110252

Contents lists available at ScienceDirect

Engineering Fracture Mechanics

journal homepage: www.elsevier.com/locate/engfracmech

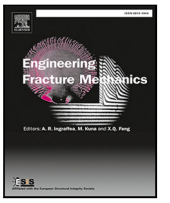

Damage mechanics challenge: Predictions from an adaptive finite element implementation of the stress-based phase-field fracture model

Abhinav Gupta [a], Duc Tien Nguyen [a], Hirshikesh [b], Ravindra Duddu [a,*]

[a] Department of Civil and Environmental Engineering, Vanderbilt University, USA
[b] Department of Mechanical Engineering, Indian Institute of Technology Jodhpur, Rajasthan 342037, India

ARTICLE INFO

Keywords:
Damage mechanics challenge
Phase field fracture
Adaptive mesh refinement
3-point bending tests
Model validation

ABSTRACT

The damage mechanics challenge (DMC) represents a critical step in predicting the damage evolution and failure in rock-like materials displaying brittle/quasi-brittle characteristics. The phase-field fracture (PFF) model is a type of damage mechanics model that is thermodynamically consistent and is well suited for capturing complex crack patterns and interactions in 3D. However, there are two main shortcomings: (1) the definition of the crack driving force function and calibration of model parameters give rise to uncertainty in predictions of load–displacement curves; and (2) the finite element implementation of the PFF model generally necessitates the use of fine meshes, leading to higher computational costs. This study presents a novel numerical methodology that employs *h*-adaptive algorithms in combination with the stress-based PFF model, and demonstrates its validity against experimental data, as required by the DMC. The core strength of our methodology lies in its computational efficiency derived from dynamically-adaptive local mesh refinement. The potential of our methodology is further demonstrated through calibration, verification, and validation studies. Our 2D and 3D simulation results show good agreement with the benchmark laboratory data from three-point bending experiments, within the bounds of data uncertainty. Our blind prediction of the 3D crack geometry for the final challenge shows good agreement with the corresponding experimental data. We find that the stress-based PFF model simplifies the parameter calibration process to a single critical stress parameter, which reduces uncertainty.

1. Introduction

Assessment and prediction of material damage pose a persistent challenge that extends across a wide range of applications in engineering and sciences, including biomedical, aerospace, marine, civil infrastructure, geothermal energy production, and glaciology. Both natural and engineering materials are susceptible to the initiation and subsequent propagation of both visible and non-visible cracks, influenced by varying operational and environmental conditions. The presence of cracks reduces the load bearing capacity and durability, emphasizing the critical significance of accurate prediction and understanding of fractures and their mechanisms. Numerous damage mechanics models and numerical methods have been proposed in the literature to predict fracture mechanisms, including crack nucleation and subsequent propagation, branching, and coalescence. While modeling approaches have become considerably advanced, their validation is somewhat limited by the lack of detailed experimental datasets.

* Corresponding author.
E-mail address: ravindra.duddu@vanderbilt.edu (R. Duddu).

https://doi.org/10.1016/j.engfracmech.2024.110252
Received 14 November 2023; Received in revised form 11 June 2024; Accepted 18 June 2024
Available online 28 June 2024

The DMC, as outlined in [1], provides an invaluable opportunity to assess, compare, and refine computational approaches for damage prediction in brittle/quasi-brittle materials. The challenge provides a standardized laboratory dataset derived from controlled three-point bending experiments on 3D printed model rock samples and offers a foundation for evaluating the accuracy and reliability of damage models. This dataset offers a comprehensive overview of material behavior and failure mechanisms through a combination of experimental techniques. Three point bending (TPB) experiments provide load–displacement calibration and digital image correlation (DIC) data for observing crack evolution. Unconfined compressive strength (UCS) and Brazilian experiments assess compressive and tensile strengths across different layer orientations, respectively. Ultrasonic measurements yield small-strain moduli and material density, essential for understanding elastic properties. Laser profilometry and 3D X-ray tomography contribute detailed analyses of surface roughness and crack geometry, including notch shapes. Altogether, this dataset integrates traditional mechanical testing with advanced imaging and profiling methods. To accurately replicate the experimental results from the DMC using numerical methods, we utilize the phase-field fracture (PFF) model, which belongs to the class of nonlocal continuum damage mechanics models.

The PFF modeling approach [2–11] uses a diffused crack representation that provides certain advantages over other fracture mechanics models using sharp crack representations, especially when it comes to capturing phenomena like crack nucleation, propagation, branching, and coalescence. Due to its advantages, this approach has been extensively used over the last decade, so a comprehensive review is beyond the scope of this article; instead, we refer the interested reader to recent review articles [12,13]. Here, we only cite a few studies that are relevant to our current implementation. The stress based PFF model considered herein was used to simulate crevasse growth in glaciers [14]. Recently, PFF models were implemented within the open-source finite element software FEniCS [15–20], which significantly reduces the burden of code development and so we use FEniCS here.

The non-convexity and non-linearity of the energy functional in PFF models add significantly to the computational cost. Additionally, the requirement for a fine mesh within the damage/fracture process zone to accurately capture the crack topology has hindered the application of PFF models in large-scale fracture simulations. To reduce computational time in brittle fracture simulations while preserving accuracy, Gupta et al. [15] presented an auto-adaptive displacement stepping algorithm. The integration of adaptive mesh refinement (AMR) algorithms with the finite element method leads to a powerful approach for tackling computational obstacles in PFF simulations. As highlighted in [21–27], AMR algorithms dynamically adapt and optimize mesh resolution for diverse fracture scenarios. Alternatively, machine learning based surrogates of the PFF model have been recently pursued with the aim of reducing computation time without much loss of accuracy [28–30], but these surrogates necessitate the generation of large training and test datasets. The AMR algorithms can offer a promising avenue for expediting the dataset generation process and accelerating the training of machine learning surrogates.

To enhance the robustness and efficiency of AMR algorithms for PFF simulation, several refinement strategies have been recently proposed. An *hp*-adaptive discontinuous Galerkin finite element method guided by error estimators was recently introduced in [31]. A locally adaptive refinement strategy with just two types of elements (standard and refined) using the variationally consistent interior penalty approach called Nitsche's method was developed in [32,33]. Within the FEniCS framework, an AMR algorithm was presented in [16] that significantly decreases computation time for brittle, cohesive, and dynamic fracture simulation. The incorporation of a multi-level conditional AMR algorithm, detailed in [16], ensures precision and efficiency by dynamically adapting the mesh to allocate computational resources where they are most critical. The purpose of this paper is twofold: (1) to calibrate and validate the stress-based PFF model with the DMC experiments by leveraging the AMR algorithm of [16] within FEniCS; and (2) to investigate sensitivity and uncertainty in predictions of load–displacement curves for the DMC experiments in relation to the model parameters. To this end, we extend the implementation of the multi-level conditional AMR algorithm of [16] for the stress-based PFF model.

The rest of this article is organized as follows: in Section 2, we introduce the approach, including details about our team, the numerical methodology employed, and the problem definition; in Section 3, we present the results of our study along with a comprehensive discussion; and in Section 4, we provide concluding remarks summarizing the key findings and insights from our studies.

2. Approach information

This section discusses our approach to predict load–displacement response and crack trajectory based on the DMC experiment.

2.1. Numerical approach

In this subsection, we describe the stress-based criteria for the PFF model, the strong and weak forms of governing partial differential equations, our solution strategy, and the AMR algorithm.

2.1.1. Stress-based phase field fracture model

The PFF model represents the damage state of a material point at position $\boldsymbol{x}$ using a scalar field variable $D(\boldsymbol{x}) \in [0,1]$, where $D = 0$ corresponds to the undamaged state and $D = 1$ corresponds to the fully damaged state. As per Griffith's theory of brittle fracture [34], the total energy stored in a cracked solid body $\Omega \subset \mathbb{R}^{[2,3]}$, illustrated in Fig. 1, can be defined based on contributions from the bulk strain energy density ψ_e and the regularized interface fracture energy ψ_f. Accounting for the work done by external tractions $\boldsymbol{T}$ on boundary $\partial\Omega$ and body forces $\boldsymbol{b}$, the total potential energy is given by,

$$\Psi_{\text{pot}} = \int_{\Omega} [\psi_e(\boldsymbol{u}, D) + \psi_f(D)] \, \mathrm{d}V - \int_{\Omega} \boldsymbol{b} \cdot \boldsymbol{u} \, \mathrm{d}V - \int_{\partial\Omega} \boldsymbol{T} \cdot \boldsymbol{u} \, \mathrm{d}S, \tag{1}$$

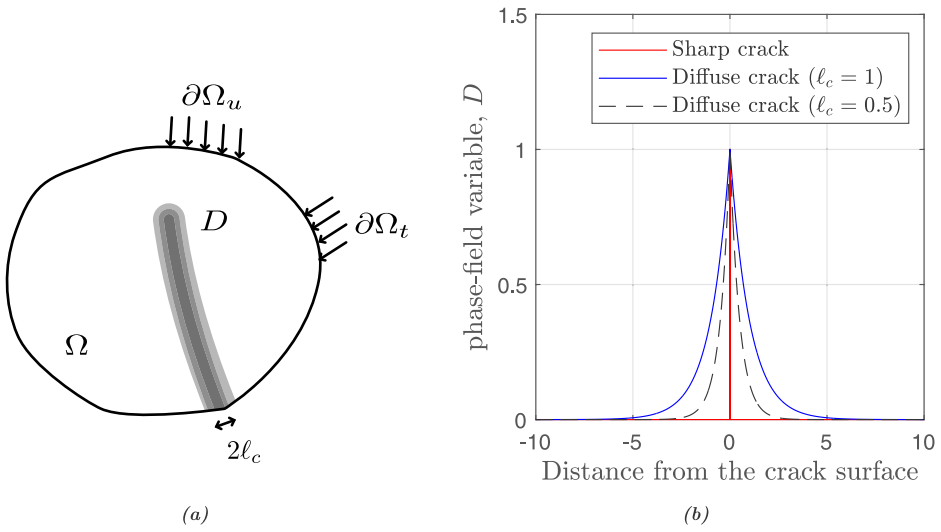

Fig. 1. Schematic of the domain Ω and the crack description within the framework of phase field fracture model.

where $\boldsymbol{u}$ is the displacement field vector. With the stress-based criterion, the degraded elastic bulk energy is defined as [35]

$$\psi_e(\boldsymbol{u}, D) = [g_d(D)(\tilde{\psi}_e(\boldsymbol{u}) - \psi_c) + \psi_c], \tag{2}$$

where the degradation function $g_d(D) = \left[(1-D)^2 + \kappa\right]$, $\kappa = 10^{-4}$ is a numerical regularization parameter, $\tilde{\psi}_e$ represents the effective strain energy density within the undamaged material and $\psi_c = 0.5\sigma_c^2/E$ is the critical strain energy density corresponding to the critical stress σ_c of the material that dictates damage initiation. The definition of the interface energy function ψ_e depends on the mechanisms of damage evolution (e.g., brittle, quasi-brittle, ductile) and loading conditions (e.g., cyclic fatigue). Here, we are only concerned with the brittle fracture of 3D printed model rock, so we employ the stress-based criterion with the interface energy expressed as [35]

$$\psi_f(D) = 2\psi_c \ell_c \gamma(D), \tag{3}$$

where $\gamma = \dfrac{D^2}{2\ell_c} + \dfrac{\ell_c}{2}|\nabla D|^2$ is the surface density function, and ℓ_c is the length scale parameter.

Substituting Eq. (3) and Eq. (2) into Eq. (1), the total potential energy can be written as,

$$\Psi_{\text{pot}} = \int_\Omega [g_d(D)(\tilde{\psi}_e - \psi_c) + \psi_c + 2\psi_c \ell_c \gamma(D)]\, \mathrm{d}V - \int_\Omega \boldsymbol{b}\cdot\boldsymbol{u}\, \mathrm{d}V - \int_{\partial\Omega} \boldsymbol{T}\cdot\boldsymbol{u}\, \mathrm{d}S. \tag{4}$$

The phase-field evolution equation is obtained by minimizing the total potential energy functional with respect to the phase field variable as,

$$\begin{aligned} \frac{\delta \Psi_{\text{pot}}}{\delta D} &= \left[\frac{\delta g_d(D)}{\delta D}(\tilde{\psi}_e - \psi_c) + 2\psi_c \ell_c \frac{\delta \gamma(D)}{\delta D}\right] = 0 \\ (\ell_c^2 \Delta D - D) &= -(1-D)\frac{(\tilde{\psi}_e - \psi_c)}{\psi_c} \end{aligned} \tag{5}$$

From the right-hand side of the above equation, the crack driving force function is defined as,

$$\mathcal{H} = \left\langle \frac{\tilde{\psi}_e}{\psi_c} - 1 \right\rangle, \tag{6}$$

where the Macaulay brackets $\langle x \rangle := (x + |x|)/2$ impose a threshold on $\mathcal{H}$ such that it acts only when $\tilde{\psi}_e > \psi_c$. The crack driving force could be rewritten in terms of stress to obtain a simple criterion for mixed tensile–compression states. To prevent compression damage, only the effective tensile stress ($\tilde{\boldsymbol{\sigma}}^+$) is considered, which is represented in terms of the principal stresses ($\tilde{\sigma}_a$) as,

$$\tilde{\boldsymbol{\sigma}}^+ := \sum_{a=1}^{3} \langle \tilde{\sigma}_a \rangle\, \boldsymbol{n}_a \otimes \boldsymbol{n}_a. \tag{7}$$

Following [35], the effective energy within the undamaged material is defined as,

$$\tilde{\psi}_e = \frac{1}{2E}\left\|\tilde{\boldsymbol{\sigma}}^+\right\|^2 = \frac{1}{2E}\sum_{a=1}^{3}\langle \tilde{\sigma}_a \rangle^2, \tag{8}$$

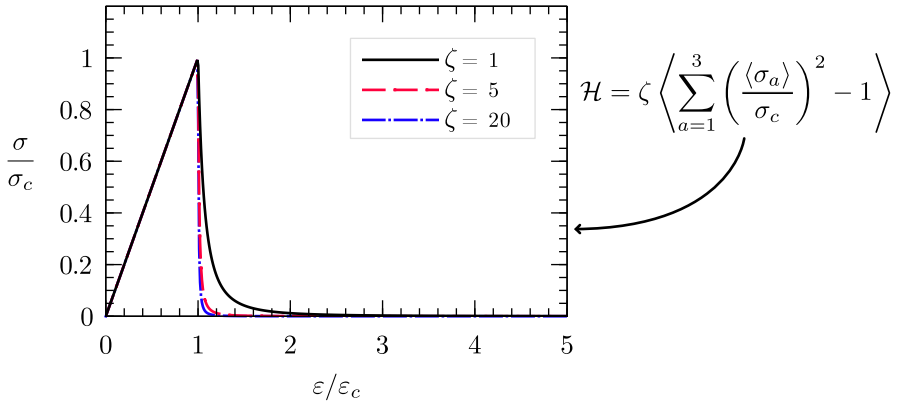

Fig. 2. Uniaxial stress–strain response predicted by the stress-based model, illustrating the influence of the post-peak parameter ζ on the material's damage softening behavior.

and the crack driving function for the stress-based criterion is given by,

$$\mathcal{H} = \left\langle \frac{\sum_{a=1}^{3} \langle \tilde{\sigma}_a \rangle^2}{\sigma_c^2} - 1 \right\rangle. \tag{9}$$

This criterion defines phase-field damage evolution to be related to the sum of the square of positive effective principal stresses. It establishes a stress threshold for the crack driving force function such that it is zero so long as $\|\tilde{\boldsymbol{\sigma}}^+\|$ is less than the material strength parameter, σ_c.

An additional dimensionless parameter $\zeta > 0$ was introduced in [35] to modify the slope of the stress–strain curve in the post-critical range (Fig. 2). The final form of the crack driving force is given by,

$$\mathcal{H} = \zeta \left\langle \frac{\tilde{\psi}_e}{\psi_c} - 1 \right\rangle = \zeta \left\langle \left(\frac{\sum_{a=1}^{3} \langle \tilde{\sigma}_a \rangle^2}{\sigma_c^2} \right) - 1 \right\rangle. \tag{10}$$

2.1.2. Material model

Our main assumption is that within the loading regime the 3D printed model rock material behaves like a linear elastic material before damage initiation. Based on the hypothesis of strain equivalence, the effective stress can be defined as

$$\tilde{\boldsymbol{\sigma}}(\boldsymbol{u}) = \frac{\partial \tilde{\psi}_e}{\partial \boldsymbol{\varepsilon}} = [\lambda \operatorname{tr}(\boldsymbol{\varepsilon}) \boldsymbol{I} + 2\mu \boldsymbol{\varepsilon}], \tag{11}$$

where $\boldsymbol{I}$ represents the identity tensor, $\boldsymbol{\varepsilon} = \operatorname{sym}(\nabla \boldsymbol{u})$ is the small strain tensor, λ and μ are the Lamé parameters that can be calculated using the Young's modulus E and the Poisson's ratio ν. The Cauchy stress tensor $\boldsymbol{\sigma}$ is defined as

$$\boldsymbol{\sigma}(\boldsymbol{u}, D) = \frac{\partial \psi_e}{\partial \boldsymbol{\varepsilon}} = g_d(D)[\lambda \operatorname{tr}(\boldsymbol{\varepsilon}) \boldsymbol{I} + 2\mu \boldsymbol{\varepsilon}], \tag{12}$$

where degraded elastic bulk energy (ψ_e) is defined as per Eq. (2).

2.1.3. Strong form of governing equations

The crack propagation problem involves determining two unknown fields: the displacement field $\boldsymbol{u}$ and the phase field variable D, representing isotropic damage. The displacement field $\boldsymbol{u}$ is obtained by solving the strong form of the equilibrium equation as given by:

$$\begin{aligned} \nabla \cdot \boldsymbol{\sigma} + \boldsymbol{b} &= \boldsymbol{0} \qquad \text{in } \Omega, \\ \boldsymbol{u} &= \boldsymbol{u}^* \quad \text{on } \partial\Omega_{\mathrm{u}}, \\ \boldsymbol{\sigma} \cdot \boldsymbol{n} &= \boldsymbol{T} \quad \text{on } \partial\Omega_{\mathrm{t}}, \end{aligned} \tag{13}$$

where $\boldsymbol{u}^*$ represents a prescribed displacement enforced on the external boundary $\partial\Omega_{\mathrm{u}}$, $\boldsymbol{T}$ is the traction acting on the external boundary $\partial\Omega_{\mathrm{t}}$, the domain boundary $\partial\Omega = \partial\Omega_{\mathrm{u}} \cup \partial\Omega_{\mathrm{t}}$, and $\boldsymbol{n}$ denotes the unit normal to the boundary of Ω, pointing outward from Ω. The above equation can be derived by minimizing the potential energy in Eq. (4) with respect to $\boldsymbol{u}$. From Eq. (5), the strong form of the scalar phase field equation along with the boundary conditions are:

$$\begin{aligned} \ell_c^2 \Delta D - D + (1 - D)\mathcal{H} &= 0 \qquad \text{in } \Omega, \\ \nabla D \cdot \boldsymbol{n} &= 0 \quad \text{on } \partial\Omega. \end{aligned} \tag{14}$$

2.1.4. Weak form of governing equations

The Galerkin weak form for the governing partial differential equations is defined as: Find $\boldsymbol{u} \in \mathcal{V}$ and $D \in S$ such that

$$\int_{\Omega} \boldsymbol{\sigma}(\boldsymbol{u}, D) : \nabla \boldsymbol{v} \, \mathrm{d}\Omega = \int_{\Omega} \boldsymbol{b} \cdot \boldsymbol{v} \, \mathrm{d}\Omega, \tag{15}$$

$$\int_{\Omega} (1 + \mathcal{H}) D\omega \; + \ell_c^{\,2} \, \nabla D \nabla \omega \, \mathrm{d}\Omega = \int_{\Omega} \mathcal{H}\omega \, \mathrm{d}\Omega, \tag{16}$$

where $\boldsymbol{u}$ and D represent trial functions associated with the displacement and phase field variables, whereas $\boldsymbol{v}$ and ω represent the corresponding test functions, respectively. The appropriate vector and scalar function spaces corresponding to displacement vector and scalar phase field variable are represented by $\mathcal{V}$ and S, respectively. The crack driving function is evaluated on a discontinuous Galerkin space with one degree of freedom per element, which alleviates the numerical issue of damage zone widening.

2.1.5. Solution strategy

In the PFF modeling approach, usually, a static displacement-controlled iterative technique known as alternate minimization [36] is employed. This approach involves incrementally increasing the applied displacement and iteratively solving the coupled equations Eqs. (15) and (16) until convergence is achieved. To guarantee the irreversibility of crack propagation, the crack driving force $\mathcal{H}_{i+1}$ at the displacement step $i+1$ must satisfy the following condition:

$$\mathcal{H}_{i+1} = \begin{cases} \mathcal{H}_{i+1} & \text{if } \mathcal{H}_{i+1} > \mathcal{H}_i \\ \mathcal{H}_i & \text{otherwise.} \end{cases} \tag{17}$$

Within the alternate minimization framework, the current approximations for the displacement and damage fields are determined based on the approximations made in the preceding step. Let $\boldsymbol{u}^j$ and D^j denote the displacement and damage fields at the end of the previous alternate minimization step, whereas $\boldsymbol{u}^{j+1}$ and D^{j+1} represent their approximations at the current alternate minimization step. The $\mathcal{L}^2$ error norms r_u and r_d corresponding to displacement and damage fields are defined as,

$$r_u = \|\boldsymbol{u}^{j+1} - \boldsymbol{u}^j\|_2 \quad \text{and} \quad r_d = \|D^{j+1} - D^j\|_2 \tag{18}$$

where $\|.\|_2 := \sqrt{\int (.)^2 \mathrm{d}x}$ represents the $\mathcal{L}^2$ norm. Alternate minimization iterations for displacement step $i+1$ will proceed until the following criteria [15] is met

$$\max(r_u, r_d) < 10^{-5} \quad \text{or} \quad j > 10. \tag{19}$$

After achieving convergence in the alternate minimization step, the applied displacement is incremented and the process of alternate minimization is repeated. The number of iterations required for convergence depends on the load and displacement steps and the boundary conditions.

2.1.6. Adaptive mesh refinement

Here, we employ and extend the AMR algorithm, originally introduced in Gupta et al. [16] for the strain-based PFF model, to the proposed stress-based PFF model described in the previous section. The AMR algorithm instantiates with a coarse mesh configuration and utilizes four refinement schemes ($S_1 \circ S_2 \circ S_3 \circ S_4$). On a relatively coarse mesh, S_1 helps detect crack initiation and facilitates proper crack propagation by refining the zone ahead of the crack tip. In contrast, S_2 prevents excessive refinement in the elastic zone and S_3 ensures proper resolution of the damaged zone, whereas S_4 prevents over-refinement in areas that have already achieved the targeted $h_{\min}$. Once the mesh is refined, damage field D and crack driving force function $\mathcal{H}(\boldsymbol{u}, D)$ are interpolated to the refined mesh and the coupled system of equations are solved until convergence is achieved, as discussed in the previous section. Below we elaborate on the four refinement schemes, which are illustrated in Fig. 3.

S_1: The evolution of the damage in the PFF formulation is governed by $\mathcal{H}$, as discussed in Section 2. Before crack initiation, the solution of the equilibrium equation is unaffected by D, allowing for a reasonably accurate approximation of the displacement field using a coarse mesh. Moreover, once crack initiation occurs, D evolves predominantly in regions with high accumulation of $\mathcal{H}$. With the stress-based criterion, the threshold applied maintains $\mathcal{H} = 0$ until the effective strain energy exceeds the critical strain energy. Based on these observations, the first refinement indicator $(\mathcal{E}_1)$ evaluates the change in elastic energy for each element in the mesh as,

$$\mathcal{E}_1^{\text{ele}} = \tilde{\psi}_{\text{ele}}^{(j+1)} - \tilde{\psi}_{\text{ele}}^{j}, \qquad \tilde{\psi}_{\text{ele}} := \int_{\text{ele}} \tilde{\psi} \; \mathrm{d}\boldsymbol{x}. \tag{20}$$

Here, $\tilde{\psi}_{\text{ele}}^{(j+1)}$ represents the integral of $\tilde{\psi}$ over the element during the $(j+1)$th alternate minimization iteration, while $\tilde{\psi}_{\text{ele}}^{j}$ represents the integral of $\tilde{\psi}$ over the element in the previous jth alternate minimization iteration. This indicator is coupled with the maximum value marking strategy, where all elements with $\mathcal{E}_1^{ele}$ values exceeding $\alpha_1 \times \max(\boldsymbol{\mathcal{E}}_1)$ are marked for refinement; $0 \leq \alpha_1 \leq 1$.

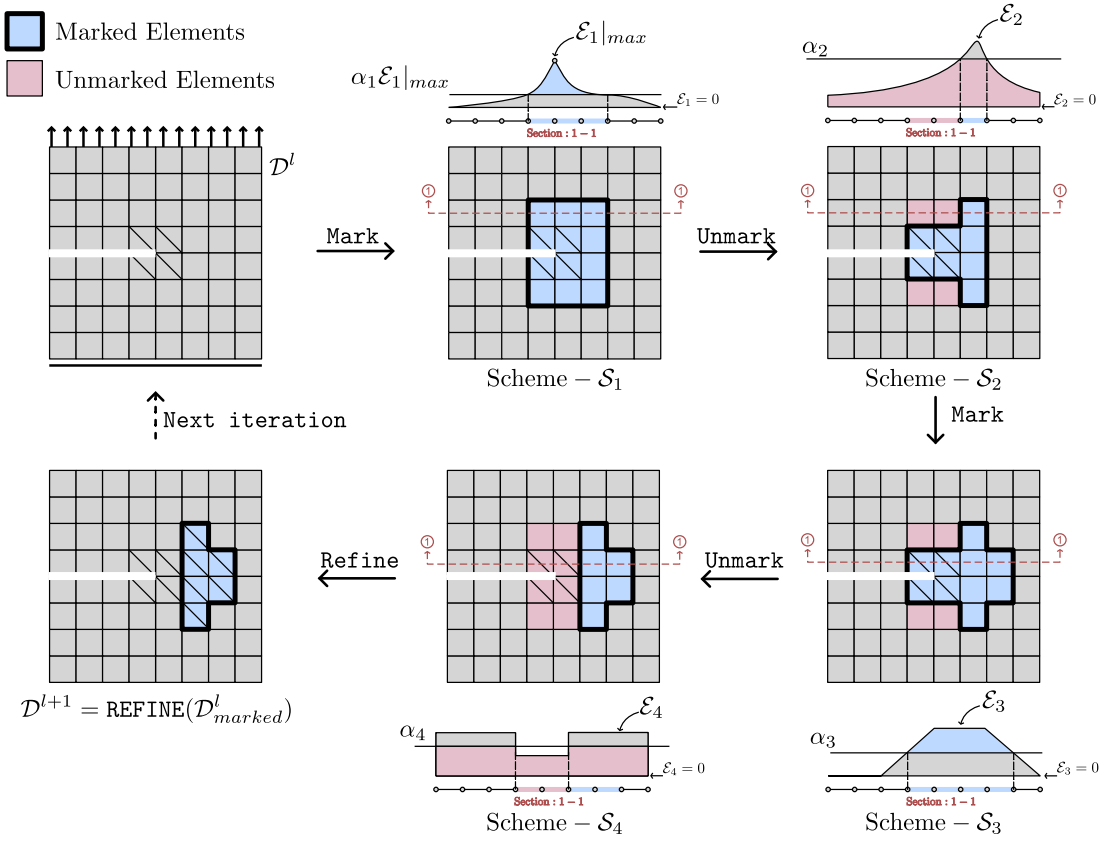

Fig. 3. Multi-level conditional AMR algorithm: This adaptive strategy employs four distinct refinement indicators, $\mathcal{E}_1$ to $\mathcal{E}_4$, utilized sequentially in combination with maximum value markers (parameter α_1 in $\mathcal{E}_1$) and threshold markers (parameters α_2, α_3, and α_4 in $\mathcal{E}_2$, $\mathcal{E}_3$, and $\mathcal{E}_4$).

$\mathcal{S}_2$: In this step, elements are unmarked based on the value of the positive component of elastic strain energy $\tilde{\psi}_e^+$. The refinement indicator at the element level is defined as follows,

$$\mathcal{E}_2^{\text{ele}} = \tilde{\psi}_e^+. \tag{21}$$

To prevent unnecessary refinement in the elastic zone, an unmark strategy is employed. Elements with $\tilde{\psi}_e^+$ values lower than the limiting strain energy ψ_c are unmarked from the set of marked elements. Elements are unmarked if $\tilde{\psi}_e^+ \leq \alpha_2\psi_c$, with a typical value of $\alpha_2 = 0.9$ for this study.

$\mathcal{S}_3$: Once damage initiation occurs, it becomes necessary to appropriately resolve the post-crack initiation damage zone according to the length scale parameter in the PFF model. To achieve this, we propose to use the damage field as a refinement indicator, The $\mathcal{E}_3$ is defined by,

$$\mathcal{E}_3^{\text{ele}} = D_{\text{ele}}. \tag{22}$$

The above scheme combined with a threshold based marking scheme marks elements with $\mathcal{E}_3$ values greater than α_3 for refinement, where α_3 ranges from 0 to 1.

$\mathcal{S}_4$: To avoid excessive refinement, we establish a specific mesh size denoted as h_{min}, which serves as the threshold (α_4) for marking elements. The selection of h_{min} depends on the parameter ℓ_c, typically so that $h_{\text{min}} \sim \ell_c/5$. Elements characterized by a diameter of the circumcircle (2×`circum_radius`) less than h_{min} are unmarked, as further refinement of these elements is deemed unnecessary. Consequently, the refinement indicator for this scheme can be expressed as follows,

$$\mathcal{E}_4^{\text{ele}} = 2 \times \texttt{circum\_radius}(\text{ele}). \tag{23}$$

The complete multi-level conditional AMR algorithm is defined as the composition of the four schemes ($\mathcal{S}_4 \circ \mathcal{S}_3 \circ \mathcal{S}_2 \circ \mathcal{S}_1$). Importantly, the order of the schemes is significant to achieve an optimal outcome.

2.1.7. Analysis software

For the analysis, we utilized an in-house code for the stress-based PFF model developed using the open-source package FEniCS v2019 [37–39]. The key selling point of FEniCS is that it uses a domain-specific language embedded into Python to specify the

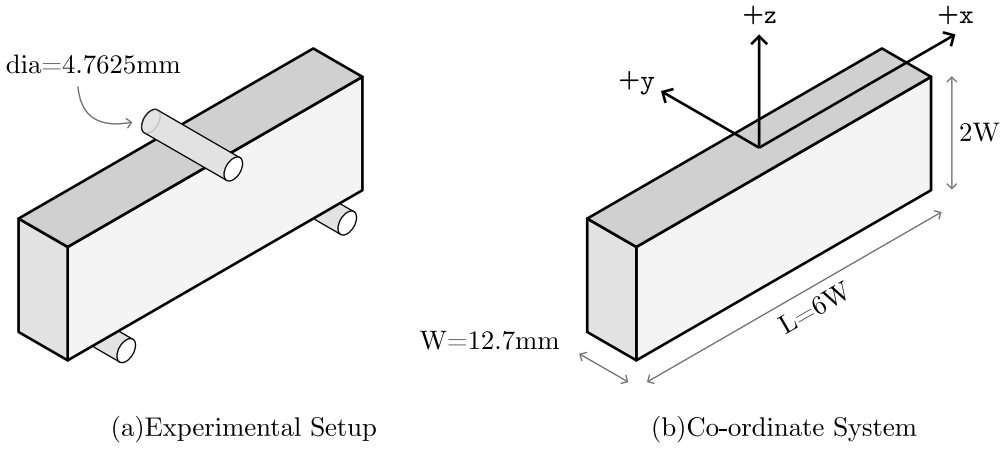

Fig. 4. Experimental setup and coordinate system orientation. (a) Cylindrical rods of dia = 4.762 mm are used to apply load and supports. (b) The coordinate system is centered on the rod on the top of the sample.

differential equation to be solved. Being open source, we are not restricted by commercial software license issues, so FEniCS can be run on massively parallel computing architectures [40,41]. The software then automatically transforms the high-level specification into an efficient, parallel C code to evaluate residual vectors and their derivatives. Under the hood, the C code uses data structures and solvers from the Portable Extensible Toolkit for Scientific Computation (PETSc), the industry standard tool for solving large systems of linear and nonlinear equations in parallel. This overall architecture allows users to write code in an environment that offers greater interactivity and immediate feedback than running batch-processed compiled programs, while still achieving the high performance of writing in a lower-level language (e.g., C or Fortran). From a performance standpoint, FEniCS includes a sophisticated optimizing compiler that can carry out loop transformations, such as sum-factorization, that are difficult to code by hand. From a usability perspective, the domain-specific language used in FEniCS maps almost directly onto the mathematical description of the variational form of the differential equation and obviates cumbersome derivations of tangent matrix and force vector.

2.1.8. Visualization software

For mesh generation, we use the open-source package Salome [42]. The simulated load–displacement response from the analysis was written to a 'CSV' file and was plotted using the open-source software VEUSZ [43]. The field variables were written to XDMF files to facilitate comprehensive visualization and post-processing. We employed an open-source multiple-platform application ParaView [44] to effectively visualize the results in 2D and 3D. Thus, we use all open-source software for both analysis and visualization, because we adhere to FAIR [45] (findability, accessibility, interoperability and reusability) principles for scientific software management.

2.2. Defining the problem

In this section, we describe the material model, boundary conditions (BCs) and mesh discretization. The fracture challenge specimen geometry with detailed dimensions is shown in Fig. 4. Three-point bending tests were conducted on 3D-printed gypsum specimens with dimensions of $25.4 \times 76.2 \times 12.7$ mm^3. Four different notch specimens were considered, as described in Fig. 7. The challenge problem is to employ a robust damage mechanics based approach to predict failure loads and crack propagation paths influenced by intentionally designed notches using the calibration, validation and blind challenge datasets.

2.2.1. Boundary conditions

In the experimental setup, Liyang et al. [1] incorporated three aluminum rods, as depicted in Fig. 4. These rods have a diameter of 4.7625 mm and a length of 19.05 mm. Precisely, one rod was placed at the top center of the sample, while the other two were positioned at the bottom, with each rod located 10% of the sample's length away from the respective end (Fig. 4). When dealing with modeling the cylindrical rod contact, addressing stress concentration at contact points is crucial. One practical approach to mitigate this concern is the utilization of Hertz contact theory [46], which deals with the contact behavior between non-conforming surfaces by considering elastic deformation to prevent infinite stresses in forced contacts and maintaining frictionless, non-adhesive interactions (see Fig. 5).

Here, we consider the support aluminum cylinders are characterized by Young's modulus $E_1 = 70,000$ MPa and Poisson's ratio $\nu_1 = 0.33$. The beam under consideration is 3D printed using gypsum, characterized by a lower Young's modulus $E = 400$ MPa and a Poisson's ratio $\nu_2 = 0.2$. Utilizing Hertz contact theory, which addresses the behavior of non-conforming surfaces in contact, we

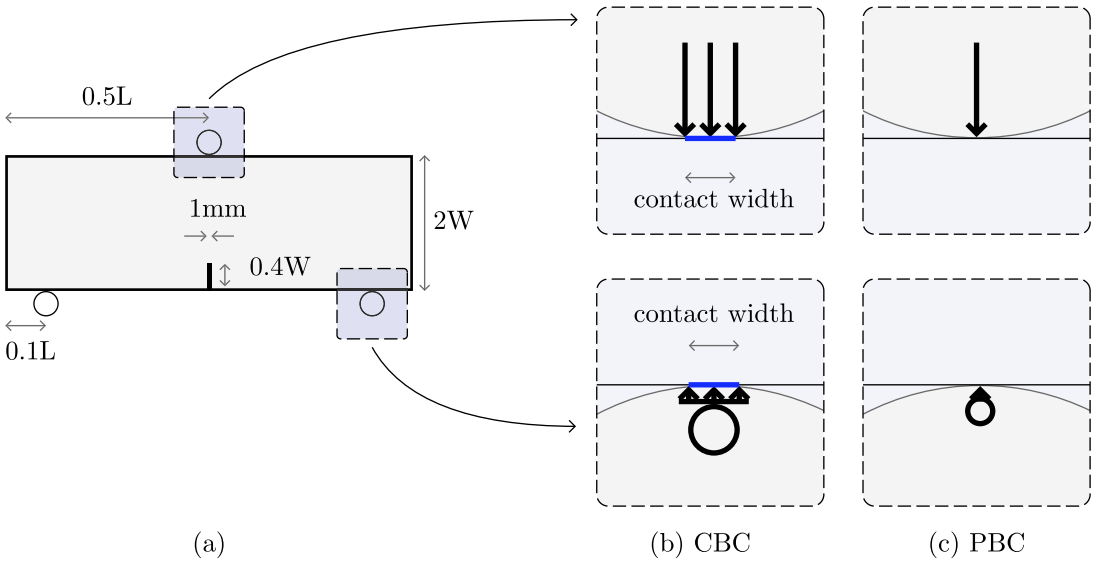

Fig. 5. Idealization of the loading and contact conditions. Point boundary condition (PBC) simplifies the representation of support and load application from cylinders by considering them as point forces and constraints. In contrast, the contact boundary condition (CBC) distributes the forces and constraints over the contact width. The latter approach provides a more accurate representation of stress and deformation distribution within the contact area.

Table 1
Load error convergence study upon mesh refinement for 2D plain strain for specimen-HC. Material properties: ($E = 400$ MPa, and $\nu = 0.2$). The errors are calculated between consecutive refined meshes. Point boundary condition (PBC) has a relative error of more than 5% at the finest level meshes, whereas, for contact boundary condition (CBC), we get a relative error of less than 5% at the coarsest level meshes, thus illustrating the benefit of CBC over PBC.

Maximum mesh	PBC		CBC	
resolution (mm)	Reaction (N)	rel. error (%)	Reaction (N)	rel. error (%)
8	109.7	–	88.25	–
4	94.47	13.9	84.83	3.9
2	85.23	9.8	82.72	2.5
1	78.59	7.8	81.59	1.4
0.5	73.31	6.7	80.89	0.9

analyze the interaction between these two distinct materials — aluminum cylinders and gypsum beam. The contact width (cw) for a cylinder and flat surface in contact is given by,

$$cw = 2 \times \sqrt{\frac{2F}{\pi l} \frac{(1-\upsilon_1^2)/E_1 + (1-\upsilon^2)/E}{1/d_1}} \tag{24}$$

where d_1 is the diameter of the aluminum cylinder, $F = 400$ N is the applied force (which is the maximum observed load in experiments, see Fig. 7) and $l = 12.7$ mm is the contact length along the y-axis.

With the assumed material properties, the Hertz contact condition in Eq. (24) yields a contact width of approximately 0.96 mm. The maximum contact pressure P over the contact area is given as

$$P = \frac{4F}{\pi cwl}. \tag{25}$$

We next conduct a convergence study to assess whether it is appropriate to replace the cylindrical rods with point loads and constraints or to treat them as Hertzian contact pressure and constraints with a width equal to $cw = 0.96$ mm. We discretize the contact zone with five elements to resolve the contact area. Table 1 presents the load error convergence study with mesh refinement using two different idealizations of loading and contact conditions for specimen HC. When we employ point conditions, stress tends to accumulate and concentrate at the discrete points where the load and support conditions are applied. In contrast, contact conditions distribute the loading over a finite width, eliminating unrealistic stress concentration and leading to more accurate results, even when the mesh is not very fine. From Table 1, it is evident that contact conditions outperform point conditions in terms of accuracy, especially for coarser mesh resolutions. This suggests that for the experimental setup involving cylindrical contacts for loading and

Fig. 6. Mesh quality in 2D and 3D is determined by a metric known as the "quality factor", which is calculated as twice the ratio of the radius of the incircle or insphere (r_i) to the radius of the circumcircle or circumsphere (r_c). A perfect triangle possesses a quality factor of 1, while a flat triangle would exhibit a quality factor of 0. Mesh containing poor quality elements can introduce errors and inaccuracies into the FEM analysis.

support, using Hertzian contact conditions with a coarser mesh provides more reliable results than point conditions with a finer mesh.

2.2.2. Meshing

We use first-order Lagrangian finite elements to discretize the domain and represent the primary field variables, displacement (a vector), and damage (a scalar), using appropriate function spaces. For the displacement variables in 2D, we utilize three-noded triangular elements, each associated with a vector function space featuring two degrees of freedom (DOFs) per node; whereas, in 3D, we use four-noded tetrahedral finite elements, each associated with a vector function space featuring three displacement DOFs per node. On the other hand, the damage variable in 2D and 3D is associated with a scalar function space, providing one damage DOF per node.

Mesh quality assessment is of paramount importance for alleviating numerical artifacts and achieving accurate results in finite element simulations. A well-designed mesh (see Fig. 6) with appropriate element sizing, shape, and connectivity ensures that the physical domain is properly represented in the discretized domain. Poor mesh quality, characterized by poor aspect ratio (elongated/distorted looking) elements or excessive element size variation between neighboring elements, can introduce numerical errors, inaccuracies, and convergence issues. In our analysis with the AMR algorithm, we placed a significant emphasis on establishing a good quality initial mesh based on the "quality factor" metric. We have adopted the refinement strategy proposed by Plaza and Carey [47] to enhance the mesh quality, which allows us to generate additional mesh elements during the refinement process while improving mesh quality.

2.2.3. Model calibration data

The calibration dataset, detailed in [1], include a collection of experimental fracture scenarios. These scenarios cover a wide range of fracture modes, including pure Mode I in the HC case and mixed-mode situations combining Mode I and II in the HA and HB cases, and likely combining Mode I, II and III in the H45 case (see Fig. 7). The primary difference between these specimens lies in where the notches are located and how they are aligned in the out-of-plane direction.

The samples employed in this calibration process were fabricated using a ProJet CJP 360 3D printer. These samples are made up of layers of calcium sulfate hemihydrate powder bonded together with a proprietary water-based binder, resulting in well-defined geometric dimensions: $25.4 \times 76.2 \times 12.7$ mm^3 (height $\times$ length $\times$ width) with a deliberately designed 5.08 mm (long) $\times$ 1.0 mm (wide) notch.

While plotting the experimental load–displacement curves for these various fracture scenarios (Fig. 7), we found anomalies in specific datasets (set-4 in HA and HC, set-3 in H45), where the load–displacement responses deviated noticeably from the other datasets. In these anomalous data, we notice that the load–displacement curve is shifted to the right by up to one-tenth of a millimeter. We suspect these deviations could have been caused by discrepancies in the testing process, such as the loss of contact between the sample and the strain gauge. To ensure reliability of our analysis, we chose to exclude these anomalous data from further consideration. For example, in our calibration study we only use datasets 3, 5 and 6 to estimate our model parameters and ignore dataset 4. This decision was made to maintain the consistency and trustworthiness of the dataset, ensuring that our subsequent conclusions are free from anomalies that could introduce inaccuracies to our findings.

2.2.4. Uncertainty in the model

Experimental data inherently has aleatoric or statistical uncertainty stemming from measurement errors, boundary condition variations, and material heterogeneity; this is evident from the load–displacement plots presented in Fig. 7. To capture the full spectrum of experimental and material variability and motivated by the significant scatter observed in the experimental data, we considered the lower and upper bounds of the load–displacement data to calibrate the Young's modulus E and critical stress σ_c. By considering these bounds in Section 3, we ensure that the outcomes from our model account for the statistical uncertainty inherent to the experimental data. In addition, due to the simplifying assumption of isotropic linear elasticity and isotropic damage in the stress-based PFF model, there can be epistemic or systematic uncertainty arising from the lack of knowledge of model parameters, namely the length scale ℓ_c. We address this epistemic uncertainty through parametric sensitivity studies in Section 3.1.

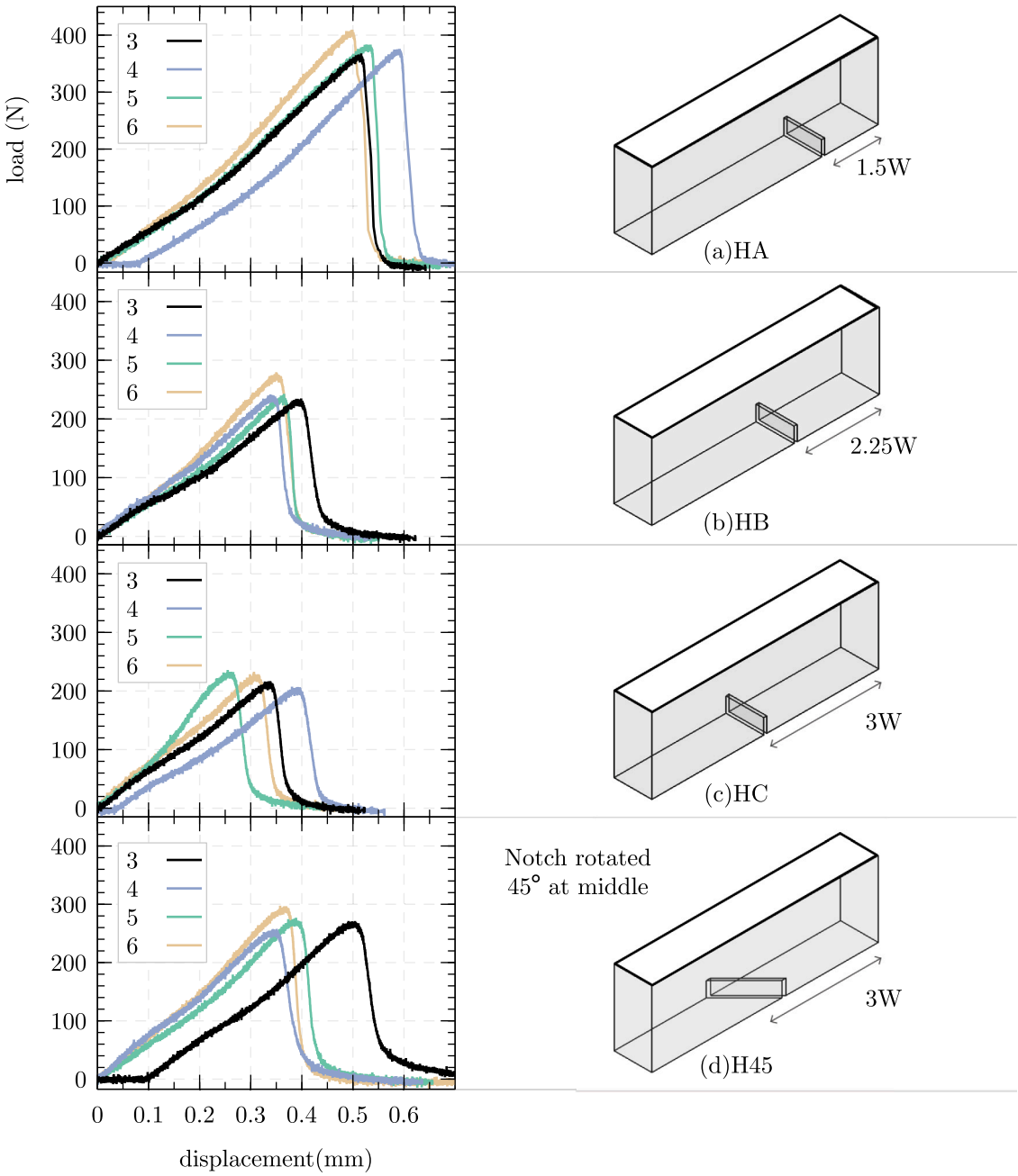

Fig. 7. Experimental load–displacement data from sets 3–6 and the specimen geometry for the HA, HB, HC, and H45 fracture scenarios. Note that anomalies in specific datasets (set-4 in HA and HC and set-3 in H45) are neglected here.

2.2.5. Model set-up and run times

All model simulations were conducted on a Windows 10 workstation equipped with 8 CPU cores and 96 GB of RAM. Our code is not parallelized and only one CPU core was utilized for the simulations. Creating all five models and meshing them in Salome required approximately four hours. Subsequently, the system was solved using an in-house code using FEniCS, and the run times for each simulation are listed in Table 3.

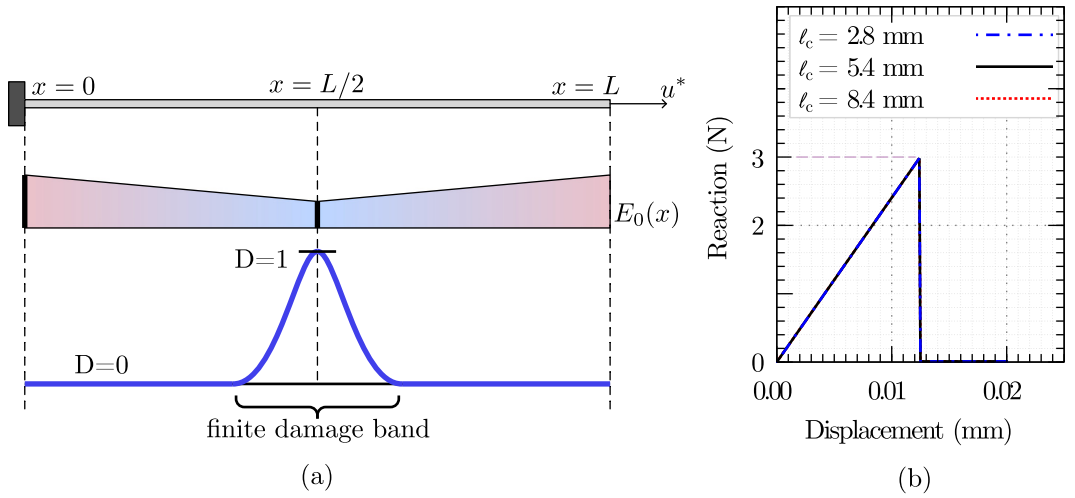

Fig. 8. Uniaxial bar: (a) Geometry and loading (b) Reaction force vs. displacement graph for different length scale. Phase field model based on stress-based crack driving function, displays a linear pre-peak behavior. Additionally, this model exhibits a finite damage band and showcases length scale independence.

3. Results and discussion

In this section, we present the results obtained from the PFF model and AMR algorithm for the verification, calibration, validation and challenge problems. The goal is to demonstrate that it is possible to achieve a good match with experimental results with fewer computational resources and/or at a lesser cost using the adaptive PFF algorithm. Unless otherwise specified, the plane-strain assumption is made in all 2D simulations. In all examples, unless otherwise specified, the following marking parameters are used in the AMR algorithm: $\alpha_1 = 0.6$, $\alpha_2 = 0.9$, $\alpha_3 = 0.01$, and $\alpha_4 = h_{\min} = \ell_c/5$ for schemes S_1 to S_4, respectively.

3.1. Length scale sensitivity

The sensitivity of a model's response to its parameters is a critical aspect in material modeling and simulation. When calibrating with experimental data, the model must exhibit a level of robustness, meaning that it should not be susceptible to spurious sensitivity to its input parameters. Such sensitivity complicates the calibration process, making it difficult to match model predictions with experiments. An ideal model strikes a balance where it remains responsive to changes in physical parameters that genuinely influence material behavior while maintaining a degree of insensitivity to numerical or regularization parameters that only serve the purpose of improving convergence or efficiency. This balance ensures that the model can be reliably calibrated for predicting material response under different conditions.

As described by Eq. (10), the crack driving force function in the stress-based PFF model is dependent only on two parameters σ_c and ζ. The parameter $\zeta \geq 1$ controls the post peak softening behavior of the load–displacement response (Fig. 2). However, our primary focus lies on accurately capturing the peak load and crack path, which ζ does not influence. To simplify the calibration process and reduce the complexity associated with multiple parameters, we take $\zeta = 1$ as a constant across all simulations. Crack initiation occurs when the stress state of the material point surpasses a failure surface in the principal stress space, which is determined by the material strength, σ_c as described in Section 2.1.

To investigate the behavior of the stress-based PFF model, we utilize the 1D bar under displacement controlled uniaxial tension, as depicted in Fig. 8. This problem serves as a cost-effective benchmark frequently employed to evaluate PFF implementations and was used in other studies [48,49]. In this test case, the bar is fixed at one end and subjected to displacement in positive x direction from the other end, as illustrated in Fig. 8. The geometric and material parameters are adopted from [16]. The critical stress σ_c is assumed to be 3 MPa and the cross-sectional area is assumed to be 1 mm^2, resulting in a peak load capacity of 3 N. As shown in Fig. 8, the stress-based PFF model accurately predicts the peak load, exhibiting a linear elastic response prior to reaching the peak. This linear response is attributed to the presence of a threshold in the crack driving force function.

As per Eq. (10), the crack driving force in the stress-based PFF model is independent of the length scale parameter. The practical implications of this length scale independence are profound. It streamlines the calibration process, by reducing it to one material parameter that is directly related to material strength, namely the critical stress σ_c. Thus, the stress-based PFF model offers a more reliable approach as it alleviates spurious sensitivity to the length scale parameter.

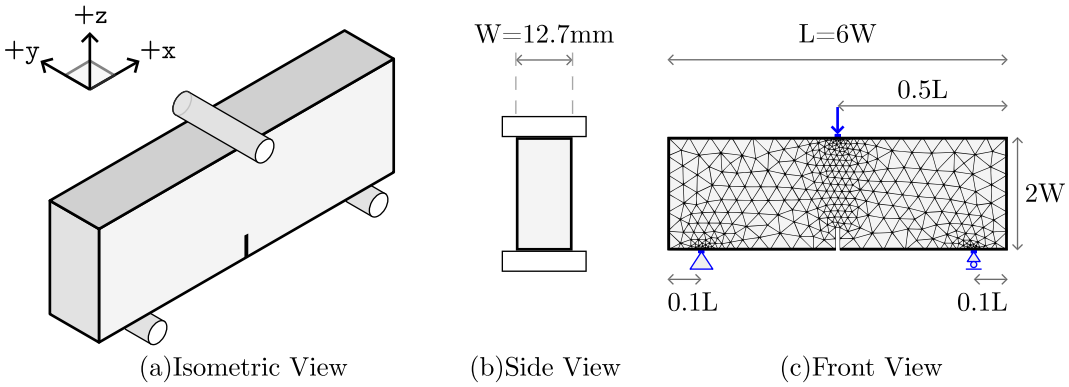

Fig. 9. Specimen HC: The three-point bending specimen with a center crack was loaded and supported using cylindrical rods having a diameter of 4.7625 mm.

3.2. Model calibration

The calibration process involves a simple trial-and-error approach to adjust the material and PFF model parameters to match the load–displacement response observed in the experimental data. Here, we perform model calibration using the HC specimen data. We begin with the determination of the material model parameters, Young's modulus E, by matching the linear (pre-damage) portion of the load–displacement curve. Subsequently, we calibrate the critical stress for damage initiation σ_c, by matching the peak load and the corresponding displacement. Importantly, the stress-based PFF model must capture the steep drop in load in the post-peak softening region of the load–displacement curve. The analysis is carried out under the assumption of 2D plane strain, and the cylindrical rods used for support and loading (see Fig. 9(a)) are idealized as line sub-domains with a length of 0.96 mm, as discussed in Section 2.2.1. The mesh is locally refined at the support and load locations with an element size of 0.1 mm, and a maximum element size of 5 mm elsewhere in the domain.

3.2.1. Calibration of Young's modulus

We presume that the gypsum's mechanical behavior resembles that of a typical rock, which generally exhibits a Poisson's ratio ranging from 0.1 to 0.3 [50,51]. To simplify calibration, we adopt a Poisson's ratio of 0.2 for the material. We calibrate Young's modulus E using experimental data and conduct a parametric study using displacement-controlled loading. Other than of the notch location, the beam geometry along with its boundary conditions and loading remain the same throughout all experiments. The Young's modulus, which is a property of the material, must be consistent across all tests, which is evident from the experimental curves, where the initial slope of the load–displacement curves is the same for all experiments, within the bounds of experimental uncertainty (Fig. 10). Consequently, we first calibrate Young's modulus using the unnotched geometry (Fig. 4) with the experimental results of HC specimen (Fig. 10(a)) and then validate it using HA, HB and H45 specimens (Fig. 10(b)). To initiate the analysis, a prescribed displacement of 0.1 mm was applied at mid-span on the top surface of the specimen in one step. This displacement induced the corresponding reaction load at the supports, allowing us to capture the pre-damage response for different Young's modulus values.

By conducting a series of simulations, we investigated the model's ability to reproduce the experimental data with different Young's modulus values. After thorough investigation, we determined that the optimal value for Young's modulus must lie within the range $E = 430$ MPa (lower bound) and $E = 630$ MPa (upper bound) for HC specimen (Fig. 10a). However, we find that load predictions with the lower bound value match better with the data from HA, HB and H45 specimens (Fig. 10b).

3.2.2. Calibration of critical stress

The precise calibration of σ_c is crucial for fracture simulation, as it significantly impacts the PFF model's ability to accurately predict the peak load capacity of the structure. By comparing our computational predictions with experimental data, here we aim to identify the most appropriate value for σ_c.

We vary σ_c while keeping ℓ_c constant at a value of 0.5 mm. The selection of a characteristic length scale parameter, $\ell_c = 0.5$ mm, is based on the understanding that the stress-based model exhibits insensitivity to the length scale and given that the notch width is significantly smaller than the size of the domain, we have selected the length scale to be half the width of the notch. For this study, we perform a displacement-controlled alternate minimization analysis with a step size of 0.06 mm, ultimately reaching a final displacement of 0.6 mm. Following a thorough investigation, we determined the most suitable parameter pairs to capture the upper bound data are $E = 630$ MPa and $\sigma_c = 8.8$ MPa, and those for the lower bound data are $E = 430$ MPa and $\sigma = 7.7$ MPa, as shown in Fig. 11 (see Table 2).

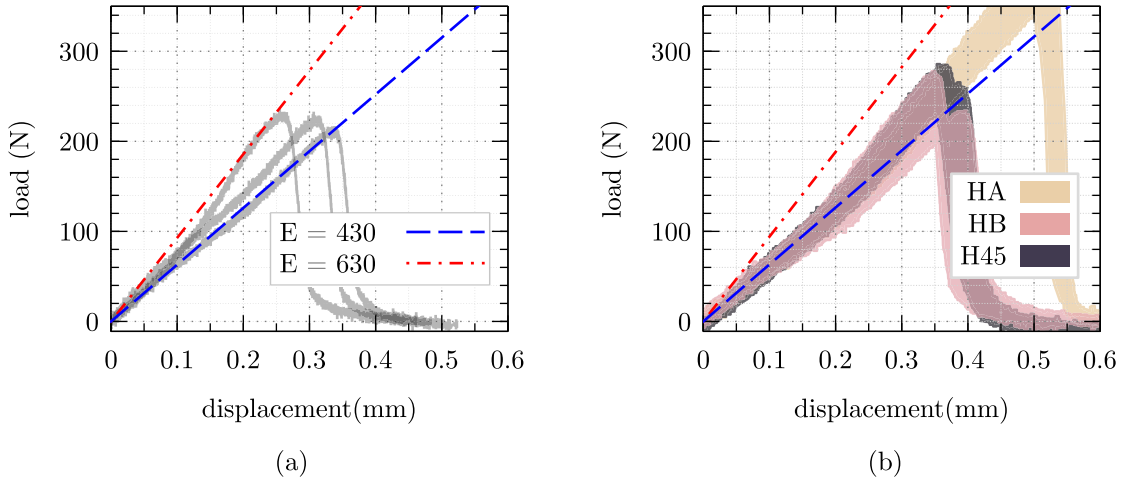

Fig. 10. Calibration study for Young's modulus E. (a) The optimal range for E that yields the closest match between our computational predictions and experimental data lies between $E = 430$ MPa (lower bound) and $E = 630$ MPa (upper bound). (b) Lower bound of E coincides well with the experimental data from other specimen geometries.

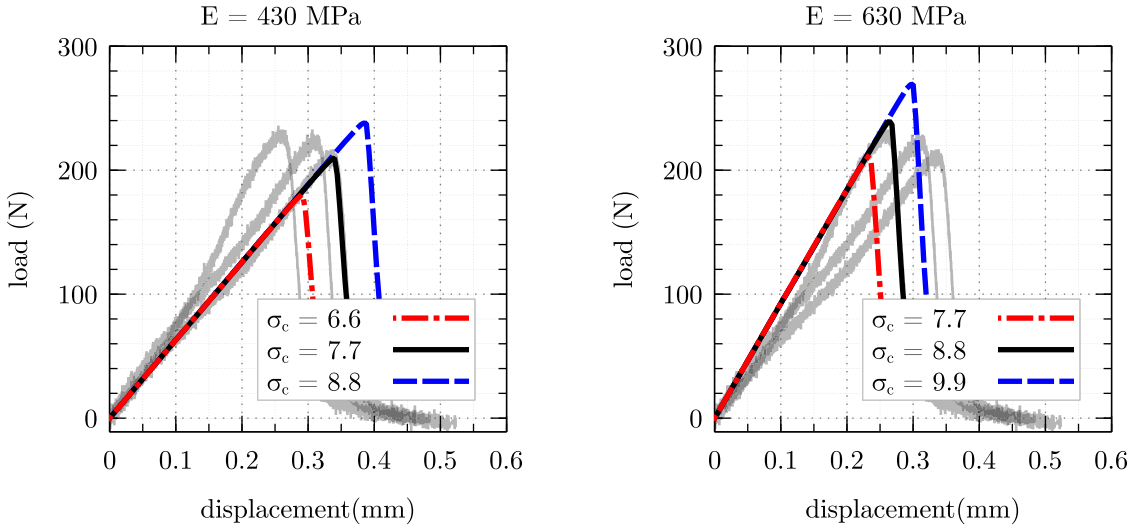

Fig. 11. Calibration study for critical stress parameter σ_c based on peak load capacity. (a) For $E = 430$ MPa, $\sigma_c = 7.7$ MPa, and (b) For $E = 630$ MPa, $\sigma_c = 8.8$ MPa.

Table 2
Calibrated material properties.

Bound	E_0 [MPa]	ν_0 [–]	σ_c [MPa]	ζ [–]
Lower	430	0.2	7.7	1
Upper	630	0.2	8.8	1

3.3. Model validation

To establish the validity of the calibrated parameters, we consider the experimental data from all four specimens HA, HB, HC, and H45. In Fig. 12, the upper and lower bounds of the load–displacement responses and crack/damage trajectories, obtained using the stress-based PFF model, are compared with the corresponding experimental data. Given that no significant change in the crack path was observed between the upper and lower bound simulations, a single figure details the crack comparison. The match between our simulation results and the experimental data is quite good. These results provide compelling evidence of the robustness of the PFF model in faithfully reproducing a wide range of experimental observations involving mixed-mode scenarios.

The complex 3D shape of specimen H45 requires 3D simulation, as a 2D representation is insufficient to accurately capture the notch details. However, conducting 3D simulations presents formidable challenges for meshing and analysis due to the small

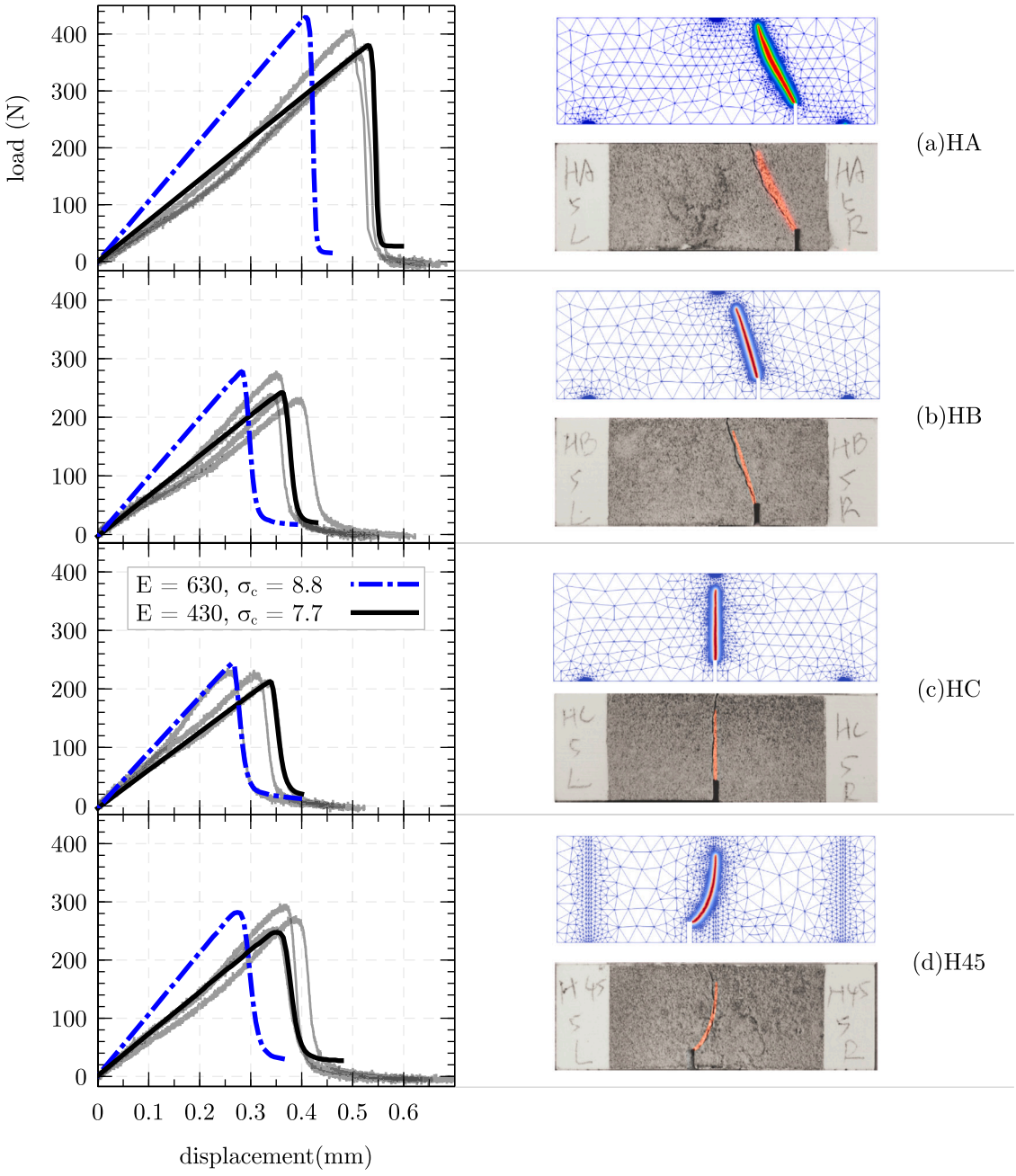

Fig. 12. Load–displacement curves and crack morphologies for HA, HB, HC, and H45 geometries. The red lines represent the cracks as the overlay of phase-field damage over actual experimental photographs. We also show the corresponding mesh generated by the AMR algorithm. The good match between simulation results and experimental data establishes the viability of the stress-based PFF model.

element size requirement of the PFF model. The requirement to employ small element sizes arises from a constraint imposed by the length scale parameter in the PFF model. This parameter mandates that the element size be less than one-fourth of the length scale at the least, with some researchers using an element size equal to one-tenth of the length scale for linear triangles [49]. In the case of specimen H45, attempting to refine the entire computational domain with elements as small as 0.1 mm ($= \ell_c/5$) would result in a highly refined mesh comprising a staggering 209 million elements, which can be prohibitively expensive. To mitigate this computational burden, local refinement can be applied specifically within the zone where crack propagation occurs, situated between the two crack faces on the front and back of the specimen. This approach significantly reduces the number of elements in the finite element mesh to a more manageable 41 million. Even this analysis still demands substantial computational resources, but

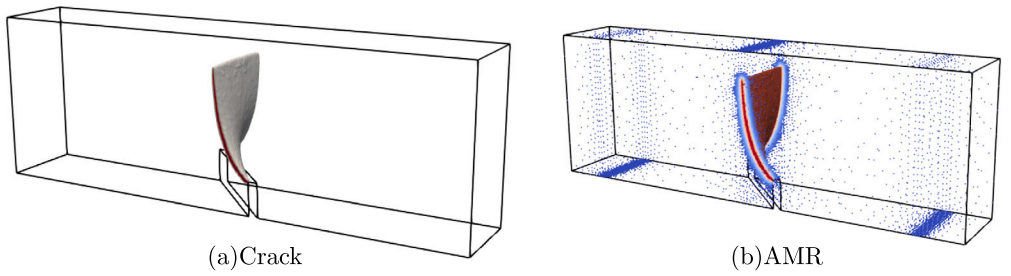

Fig. 13. Simulation results for H45 specimen. (a) 3D crack morphology. (b) Adaptively refined mesh at the final step. The elements are omitted for the sake of visibility; only the nodes are shown as a point cloud.

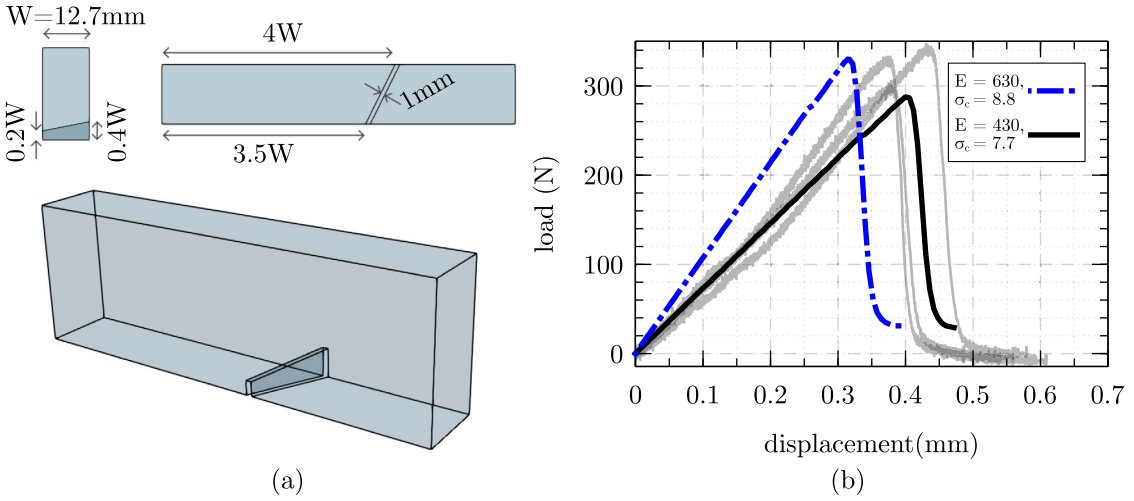

Fig. 14. 3D geometry and load–displacement curves for the challenge problem. The lower and upper bound values of the parameters, obtained from our calibration exercise, yielded a predicted peak load of 287 N and 330 N, respectively.

more importantly it requires *a priori* knowledge of the final crack path. It is therefore likely that the user refines the mesh based on a guestimate of the final crack path, and if wrong must rerun the analysis with a more appropriate mesh discretization.

In contrast, our AMR algorithm, implemented with a target mesh size of 0.1 mm, reduces the number of elements in the finite element mesh to a modest 2.5 million. Consequently, we are able to run the simulation in 17 h using a single core (Table 3). Parallelization maybe necessary to further enhance the efficiency of our implementation, especially in cases where multiple cracks can nucleate and propagate simultaneously and/or where the domain size is much larger than the crack width (or damage length scale). Fig. 13 shows the 3D crack path and the adaptively refined mesh, where the elements are omitted for the sake of visibility; only the finite element nodes are shown as a point cloud.

3.4. Challenge problem

The geometry of the challenge specimen features an off-center notch, and the height of the notch varies across the width of the beam, ranging from 0.4 W to 0.2 W, as illustrated in Fig. 14. The width of the notch is 1 mm and uniform along its length. The notch is positioned at a distance of 4 W from the left edge on the front face and 3.5 W on the back face. The boundary conditions applied to this specimen are identical to those used for all the calibration and validation specimens. Due to this unique geometry, it is likely that the fracture propagation occurs under general mixed-mode conditions, with Mode I still dominant over Mode II or Mode III owing to the brittle nature of the 3D printed model rock.

We used the stress-based PFF model along with the AMR algorithm to improve computational performance. The mesh was dynamically refined, finally achieving a mesh with more elements concentrated around the crack path and a minimum element size of $h_{\min} = \ell_c/5$. The model predicts a peak load with a lower bound of 287 N and an upper bound of 330 N, which have about 6% relative error compared to the experimentally observed peak loads of 304 N and 350 N (see Fig. 14b). The predicted lower bound curve (E = 430 MPa, σ_c = 7.7 MPa) matches better with its experimental counterpart, but the upper bound curve (E = 630 MPa, σ_c = 8.8 MPa) shows premature failure at a smaller displacement that its experimental counterpart. Fig. 15 shows the overlay comparison between the crack paths obtained from experiments and the PFF simulation. The experimental crack path obtained

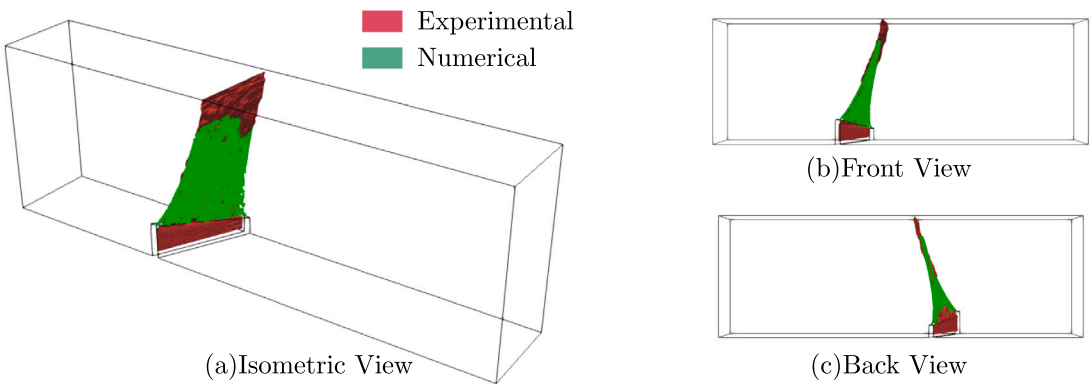

Fig. 15. Crack morphology in various perspective views for the challenge problem, showing a good match between experiments and model predictions. The numerical crack zone represents the area where the damage exceeds a value of 0.99. For an interactive 3D version of this result, please visit https://abhigupta.io/llnl-damage-challenge/.

using laser profilometry was reported in [1] using the coordinate system shown in Fig. 4. The crack surface was tracked along the x-axis on a y-z grid with a 0.1 mm resolution, which is visualized as a surface plot in ParaView. The numerical crack is a damage zone that refers to an area where the damage exceeds a value of 0.9. We are able to get a good match between the experimental and numerically predicted crack paths, except that the damage zone is a bit wider than the actual crack. Thus, the simple stress-based PFF model along with an isotropic linearly elastic material model can reasonably capture both the 3D crack morphology and load displacement response observed in the experiments. However, it may be important to consider material nonlinearity and damage-induced anisotropy to further improve the PFF model and capture the nonlinearity in the load–displacement data observed in experiments.

3.5. Discussion

This work combined the stress-based phase-field fracture (PFF) model with an AMR algorithm to address the damage mechanics challenge of accurately predicting crack propagation in 3D printed rock using the provided experimental datasets. Predicting how cracks initiate, propagate, and interact under different loading modes and specimen geometries in a precise and efficient manner is a formidable task. Although the proposed PFF model can capture crack propagation in 2D and 3D, it is important to note its strengths and limitations, as discussed below:

(i) **On calibration data:** Accurately calibrating the material model parameters is crucial for enabling predictive simulation. In this work, the Poisson's ratio of the 3D printed model was simply assumed, but data from experimental tests is needed to estimate this parameter. The calibration of the Young's modulus was based on the initial slope of the load–displacement plots provided in the calibration data. We note that a better experimental method for quantifying the Young's modulus and the Poisson's ratio is to use elastic wave propagation [52]. In most of the experimental load–displacement plots provided in the calibration dataset, an increase in the slope (stiffness) is observed with applied displacement before the load peak. This nonlinearity in stiffness of 3D printed rock was not accounted for in our study. In the rock mechanics literature, this nonlinear elastic behavior has been attributed to the presence of defects [53]; consequently, the Young's modulus of rock is different under tension and compressive stress states. However, with the simplistic assumption that 3D printed rock is linearly elastic, we calibrated the critical stress parameter in the stress-based PFF model using the provided load–displacement data. Considering material nonlinearity and damage-induced anisotropy could further improve the PFF model; however, this would also require more experimental data from different loading conditions.

(ii) **On computational cost:** The high computational cost of PFF simulations is a well-known issue; however, the AMR algorithm allowed us to conduct simulations efficiently, significantly reducing the cost. It facilitated the calibration of the model parameters through simple trial-and-error procedure, by expediting the simulations. The capability to try several parameter values and assess their impact on the model predictions was essential to ensuring model reliability. Furthermore, AMR played a pivotal role in our ability to predict the 3D crack morphology in the challenge problem case. Without AMR, the computational cost for achieving such predictions using uniformly refined meshes could be cost-prohibitive, both in terms of time and resources. From Table 3 it is evident that the calibrated PFF model often produced predictions that closely match with experimental results, with less than 5 percent error in HA, HB and HC cases, and around 10 percent relative error in the H45 and challenge problem cases. Thus, using AMR allowed us to accomplish our goal of establishing the viability of the stress-based PFF model for brittle/quasi-brittle fracture in rocks.

(iii) **On uncertainty:** Even though 3D printed rock was produced under controlled laboratory conditions, it seems that the inherent lack of uniformity in the binding process may have lead to heterogeneity in the porous rock microstructure. This coupled with the uncertainties in specimen geometries and other practical boundary conditions could have resulted in the variability

Table 3
Peak load values for all specimen configurations. A comparison is made between the upper and lower bounds from experiments (*exp*) and simulations (*sim*). Relative errors and run times are also reported.

	Lower bound			Upper bound			Run-time
	exp (N)	*sim* (N)	*Rel. err*%	*exp* (N)	*sim* (N)	*Rel. err*%	
Specimen - HA	368	380	3.2	410	430	4.88	723 s
Specimen - HB	234	241	2.99	280	276	−1.42	912 s
Specimen - HC	207	209	0.97	236	236	0.0	745 s
Specimen - H45	257	229	−10.89	297	261	−12.12	17 h
Specimen - DMC	304	287	−5.59	350	330	−5.71	20 h

observed in the load–displacement data. To account for it in the simplest manner, we calibrated the PFF model parameters using upper and lower bounds of the load–displacement data. While this simple approach acknowledges and accommodates the variability and uncertainty present in the experimental data, to address both statistical and systematic uncertainty in a sophisticated manner would involve probabilistic multi-scale modeling with micro-scale spatial randomness [54,55] and Bayesian approaches for parameter identification (e.g., [56]). Such approaches can quantitatively account for variability by considering probability distributions for model parameters and input variables. In future, as we deploy our AMR algorithm on high performance computing clusters, the stress-based PFF model offers a promising avenue to delve deeper into uncertainty in material modeling, including the issues of statistical and energetic size effects on material fracture strength [57,58].

4. Conclusion

In this work, we employed the stress-based phase-field fracture model to achieve the goals of the damage mechanics challenge. To enhance the computational efficiency of our numerical approach, we implemented a novel adaptive mesh refinement (AMR) algorithm that allows for the automatic tracking of crack trajectories and dynamically refines the mesh in the vicinity of the anticipated fracture zones.

Our participation in this challenge provided valuable insights into the capabilities and limitations of the stress-based PFF model. Numerical investigations revealed that this model is adequately robust for predicting various fracture mechanisms in complex mixed-mode fracture problems, despite the simple definition of the crack driving force function based on positive principal stresses. The model's simplicity, relying on just two parameters, Young's modulus and critical stress reduces uncertainty with calibrating to load–displacement data. In most cases, our calibrated model provided load predictions that were less than 5% or 10% relative error, which is generally acceptable for engineering, geology and geoscience applications. The combination of AMR algorithm with the PFF model brings down the computational cost significantly; for example, from an excessively refined mesh with 209 million elements to a more manageable mesh with only 2.5 million elements in the specimen-H45 case. The computational cost is often the more pressing concern for large scale simulations in engineering and science applications. For computational efficiency, we used a staggered scheme that may cause damage widening in our results. While this issue may be resolved using monolithic schemes [31,59], they can be costly and pose challenges for implementing AMR algorithms.

As we scale our model implementation to high performing computing, we are excited about the prospect of addressing challenging fracture and localized corrosion problems involving multi-scale and multi-physics interactions [60,61]. The AMR algorithm can also enable us to conduct computationally intensive Monte Carlo simulations and quantify uncertainty, which are otherwise infeasible due to the computational cost of uniformly structured meshes. This opens up opportunities to test the predictive limits of existing PFF models, and ultimately advancing them to achieve robust fracture predictions. Moreover, the implementation of our model within the open source software FEniCS ensures findability, accessibility, inter-operability and reusability (FAIR) principles, thus making computational fracture mechanics research more inclusive and broaden participation from diverse groups, including undergraduate and minority students.

CRediT authorship contribution statement

Abhinav Gupta: Writing – original draft, Visualization, Validation, Supervision, Software, Methodology, Investigation, Formal analysis, Data curation. **Duc Tien Nguyen:** Writing – original draft, Visualization, Validation, Investigation, Formal analysis, Data curation. **Hirshikesh:** Writing – review & editing, Conceptualization. **Ravindra Duddu:** Writing – review & editing, Supervision, Resources, Project administration, Funding acquisition, Conceptualization.

Declaration of competing interest

The authors declare that they have no known competing financial interests or personal relationships that could have appeared to influence the work reported in this paper.

Data availability

Data will be made available on request.

Acknowledgments

We gratefully acknowledge the funding support provided by the National Science Foundation's Office of Polar Programs via CAREER, USA grant no. PLR-1847173, and NASA Cryosphere, USA Award no. 80NSSC21K1003. Funding support from Fulbright Kalam-Climate Fellowship facilitated the collaboration with Hirshikesh.

Appendix A. Computational expense using adaptive and non-adaptive phase field fracture simulations

The computational expense associated with PFF simulations is a significant concern, especially for three-dimensional problems or scenarios involving multiple cracks. In PFF models, the crack is smeared over a zone characterized by the length scale parameter. This smearing requires the mesh to be sufficiently refined in the crack zone to accurately resolve the phase field variable. A significant challenge in simulating crack propagation is the unpredictability of the crack path in practical scenarios. Without prior knowledge of the crack path, local refinement strategies become ineffective for complex problems. Applying global refinement across the entire domain incurs a significant computational cost, making the problem virtually impractical to solve. Our proposed adaptive refinement strategy addresses this limitation by dynamically adjusting the mesh refinement based on the evolving phase field variable. This approach does not require any pre-refinement of the damage zone; instead, it automatically detects regions where the mesh needs to be refined based on the simulation's current state.

To demonstrate the benefits of our adaptive approach over the non-adaptive approach we consider the HA-specimen (Fig. 12 (a)). The mesh size for the non-adaptive case and the target mesh size for the adaptive case are kept $h_{min} = \ell/5$. We start the simulation with a relatively coarse initial mesh (4421 DoF), which gets refined by the proposed AMR algorithm when the crack starts to initiate (see Fig. A.16), thus the approach is computationally much more efficient in the initial iterations. As the crack propagates, the number of degrees of freedom (DoFs) increases, leading to longer run times per iteration due to the increased mesh resolution. The final mesh for the adaptive simulation consists of 44,097 DoFs, in contrast to the 157,618 DoFs required for the non-adaptive simulation. Owing to the significant computational efficiency gained in the pre-peak-load regime of the adaptive simulation, the total simulation time is reduced to 723 s, compared to 3233 s for the non-adaptive approach. In the non-adaptive

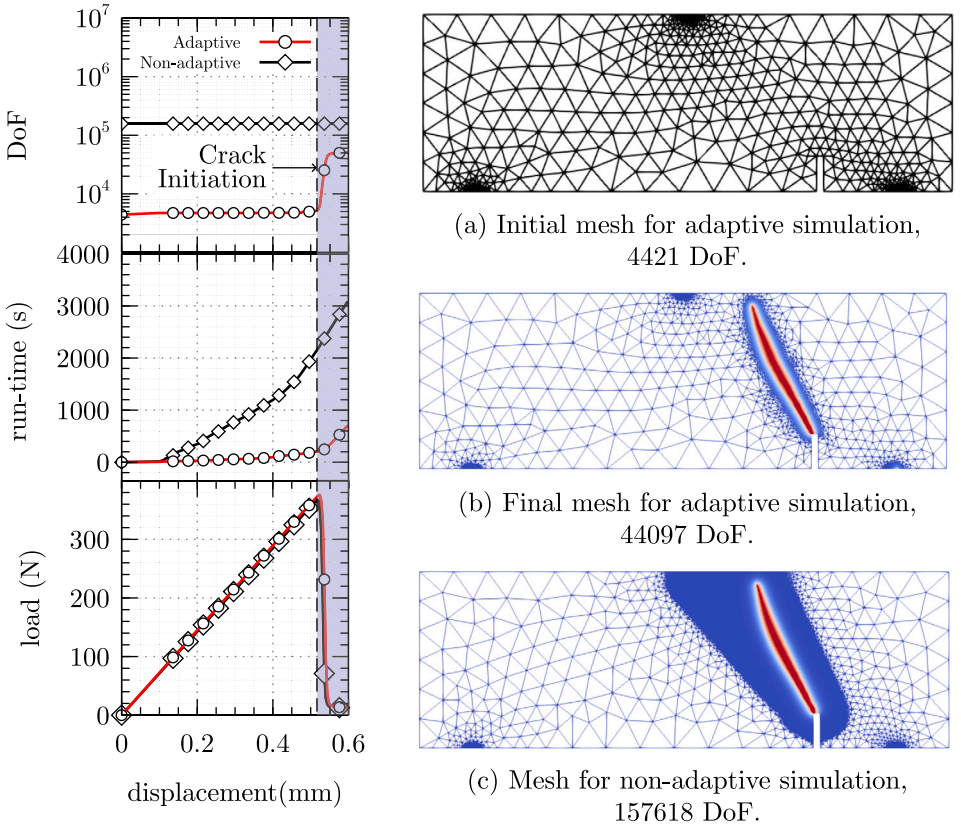

Fig. A.16. Specimen-HA: comparing results using adaptive and non-adaptive (locally refined) PFF. Minimum element size $h_{min} = \ell/5$ with $\ell = 0.5$ mm. As the crack propagates, the number of degrees of freedom (DoF) increases, leading to longer run times. The adaptive PFF model achieves the same response as its non-adaptive counterpart in 723 s, compared to the 3223 s required by the non-adaptive model.

simulation, the domain must be pre-refined along the expected crack path, whereas our proposed AMR algorithm eliminates the need for any pre-refinement. Thus, this study showcases the AMR algorithm's efficiency in accurately capturing crack initiation, and its ability to provide significant computational gains, as it allows for targeted refinement only in areas where the crack develops, optimizing both computational resources and simulation time.

Appendix B. The team

Our research team comprises Dr. Abhinav Gupta, a postdoctoral researcher at Vanderbilt University, and Mr. Duc Tien Nguyen, a Ph.D. student, along with their advisor Prof. Ravindra Duddu at Vanderbilt University, and a collaborator Prof. Hirshikesh at the Indian Institute of Technology Jodhpur. Prof. Duddu's group specializes in computational modeling of material degradation, contributing to strain and stress-based poro-damage phase field models. Dr. Gupta is an expert in computational tools for fracture problems using FEniCS, and Dr. Hirshikesh focuses on adaptive phase field methods. Together, our expertise drives the application of the PFF model to address the DMC.

References

[1] Liyang Jiang, Hongkyu Yoon, Laura J Pyrak-Nolte, Antonio Bobet, Joseph Morris. Calibration data set for damage mechanics challenge on brittle-ductile material. 2022, URL https://purr.purdue.edu/publications/3905/1.

[2] Miehe Christian, Hofacker Martina, Welschinger Fabian. A phase field model for rate-independent crack propagation: Robust algorithmic implementation based on operator splits. Comput Methods Appl Mech Engrg 2010;199(45–48):2765–78.

[3] Miehe Christian, Welschinger Fabian, Hofacker Martina. Thermodynamically consistent phase-field models of fracture: Variational principles and multi-field FE implementations. Int J Numer Methods Eng 2010;83(10):1273–311.

[4] Borden Michael J, Verhoosel Clemens V, Scott Michael A, Hughes Thomas JR, Landis Chad M. A phase-field description of dynamic brittle fracture. Comput Methods Appl Mech Engrg 2012;217:77–95.

[5] Mai Weijie, Soghrati Soheil, Buchheit Rudolph G. A phase field model for simulating the pitting corrosion. Corros Sci 2016;110:157–66.

[6] Mai Weijie, Soghrati Soheil. A phase field model for simulating the stress corrosion cracking initiated from pits. Corros Sci 2017;125:87–98.

[7] Shen Rilin, Waisman Haim, Guo Licheng. Fracture of viscoelastic solids modeled with a modified phase field method. Comput Methods Appl Mech Engrg 2019;346:862–90.

[8] Gao Huadong, Ju Lili, Duddu Ravindra, Li Hongwei. An efficient second-order linear scheme for the phase field model of corrosive dissolution. J Comput Appl Math 2020;367:112472.

[9] Gao Huadong, Ju Lili, Li Xiao, Duddu Ravindra. A space-time adaptive finite element method with exponential time integrator for the phase field model of pitting corrosion. J Comput Phys 2020;406:109191.

[10] Navidtehrani Yousef, Betegon Covadonga, Martinez-Paneda Emilio. A unified abaqus implementation of the phase field fracture method using only a user material subroutine. Materials 2021;14(8):1913.

[11] Navidtehrani Yousef, Betegon Covadonga, Martinez-Paneda Emilio. A general framework for decomposing the phase field fracture driving force, particularised to a drucker–prager failure surface. Theor Appl Fract Mech 2022;121:103555.

[12] Zhuang X, Zhou S, Huynh GD, Areias P, Rabczuk T. Phase field modeling and computer implementation: A review. Eng Fract Mech 2022;262:108234.

[13] Wu Jian-Ying, Nguyen Vinh Phu, Nguyen Chi Thanh, Sutula Danas, Sinaie Sina, Bordas Stéphane PA. Phase-field modeling of fracture. Adv Appl Mech 2020;53:1–183.

[14] Clayton Theo, Duddu Ravindra, Siegert Martin, Martinez-Paneda Emilio. A stress-based poro-damage phase field model for hydrofracturing of creeping glaciers and ice shelves. Eng Fract Mech 2022;272:108693.

[15] Gupta Abhinav, Krishnan U Meenu, Chowdhury Rajib, Chakrabarti Anupam. An auto-adaptive sub-stepping algorithm for phase-field modeling of brittle fracture. Theor Appl Fract Mech 2020;108:102622.

[16] Gupta Abhinav, Krishnan U Meenu, Mandal Tusha Kanti, Chowdhury Rajib, Nguyen Vinh Phu. An adaptive mesh refinement algorithm for phase-field fracture models: Application to brittle, cohesive, and dynamic fracture. Comput Methods Appl Mech Engrg 2022;399:115347.

[17] Krishnan U Meenu, Gupta Abhinav, Chowdhury Rajib. Adaptive phase-field modeling of brittle fracture using a robust combination of error-estimator and markers. Eng Fract Mech 2022;274:108758.

[18] Mandal Tushar Kanti, Gupta Abhinav, Nguyen Vinh Phu, Chowdhury Rajib, Vaucorbeil Alban. A length scale insensitive phase field model for brittle fracture of hyperelastic solids. Eng Fract Mech 2020;107196.

[19] Hirshikesh, Natarajan Sundararajan, Annabattula Ratna Kumar. A FEniCS implementation of the phase field method for quasi-static brittle fracture. Front Struct Civ Eng 2019;13:380–96.

[20] Sun Xiangming, Duddu Ravindra, Hirshikesh. A poro-damage phase field model for hydrofracturing of glacier crevasses. Extreme Mech Lett 2021;45:101277.

[21] Hirshikesh H, Pramod ALN, Waisman Haim, Natarajan S. Adaptive phase field method using novel physics based refinement criteria. Comput Methods Appl Mech Engrg 2021;383:113874.

[22] Zhang Tiancheng, Yu Tiantang, Xing Chen, Natarajan Sundararajan, et al. An adaptive dynamic phase-field method using the variable-node elements for cohesive dynamic fracture. Comput Methods Appl Mech Engrg 2023;416:116390.

[23] Pramod Aladurthi LN, Hirshikesh, Natarajan Sundararajan, Ooi Ean Tat. Application of adaptive phase-field scaled boundary finite element method for functionally graded materials. Int J Comput Methods 2021;18(03):2041007.

[24] Agrawal Vinamra, Runnels Brandon. Robust, strong form mechanics on an adaptive structured grid: efficiently solving variable-geometry near-singular problems with diffuse interfaces. Comput Mech 2023.

[25] Agrawal Vinamra, Runnels Brandon. Block structured adaptive mesh refinement and strong form elasticity approach to phase field fracture with applications to delamination, crack branching and crack deflection. Comput Methods Appl Mech Engrg 2021;385:114011.

[26] Mobasher Mostafa E, Waisman Haim. Adaptive modeling of damage growth using a coupled FEM/BEM approach. Internat J Numer Methods Engrg 2016;105(8):599–619.

[27] Bijaya Ananya, Gupta Abhinav, Krishnan U Meenu, Chowdhury Rajib. A multilevel adaptive mesh scheme for efficient simulation of thermomechanical phase-field fracture. J Eng Mech 2024;150(6):04024029.

[28] Gao Yuxiang, Berger Matthew, Duddu Ravindra. CNN-based surrogate for the phase field damage model: Generalization across microstructure parameters for composite materials. J Eng Mech 2023;149.

[29] Perera Roberto, Agrawal Vinamra. A generalized machine learning framework for brittle crack problems using transfer learning and graph neural networks. Mech Mater 2023;181:104639.

[30] Perera Roberto, Agrawal Vinamra. Dynamic and adaptive mesh-based graph neural network framework for simulating displacement and crack fields in phase field models. Mech Mater 2023;186:104789.
[31] Bird Robert E, Augarde Charles E, Coombs William M, Duddu Ravindra, Giani Stefano, Huynh Phuc T, Sims Bradley. An hp-adaptive discontinuous galerkin method for phase field fracture. Comput Methods Appl Mech Engrg 2023;416:116336.
[32] Jain Ishank, Muixí Alba, Annavarapu Chandrasekhar, Mulay Shantanu S, Rodríguez-Ferran Antonio. Adaptive phase-field modeling of fracture in orthotropic composites. Eng Fract Mech 2023;109673.
[33] Khan Salman, Muixí Alba, Annavarapu Chandrasekhar, Rodríguez-Ferran Antonio. Adaptive phase-field modeling of fracture propagation in bi-layered materials. Eng Fract Mech 2023;292:109650.
[34] Lajtai EZ. A theoretical and experimental evaluation of the griffith theory of brittle fracture. Tectonophysics 1971;11(2):129–56.
[35] Miehe Christian, Schaenzel Lisa-Marie, Ulmer Heike. Phase field modeling of fracture in multi-physics problems. part I. balance of crack surface and failure criteria for brittle crack propagation in thermo-elastic solids. Comput Methods Appl Mech Engrg 2015;294:449–85.
[36] Ambati Marreddy, Gerasimov Tymofiy, Lorenzis Laura De. A review on phase-field models of brittle fracture and a new fast hybrid formulation. Comput Mech 2015;55(2):383–405.
[37] Logg Anders, Mardal Kent-Andre, Wells Garth. Automated solution of differential equations by the finite element method: The fenics book, vol. 84, Springer Science & Business Media; 2012.
[38] Alnæs Martin, Blechta Jan, Hake Johan, Johansson August, Kehlet Benjamin, Logg Anders, Richardson Chris, Ring Johannes, Rognes Marie E, Wells Garth N. The fenics project version 1.5. Arch Numer Softw 2015;3(100).
[39] Logg Anders, Wells Garth N. Dolfin: Automated finite element computing. ACM Trans Math Softw 2010;37(2):1–28.
[40] Hoffman Johan, Jansson Johan, Jansson Niclas. FEniCS-HPC: Automated predictive high-performance finite element computing with applications in aerodynamics. In: Parallel processing and applied mathematics: 11th international conference, PPAM 2015, krakow, Poland, September 6-9, 2015. revised selected papers, part i 11. Springer; 2016, p. 356–65.
[41] Richardson Chris N, Sime Nathan, Wells Garth N. Scalable computation of thermomechanical turbomachinery problems. Finite Elem Anal Des 2019;155:32–42.
[42] Ribes Andre, Caremoli Christian. Salome platform component model for numerical simulation. In: 31st annual international computer software and applications conference. COMPSAC 2007, vol. 2, IEEE; 2007, p. 553–64.
[43] Sanders Jeremy. Veusz scientific plotting package. Astrophysics Source Code Library; 2023, p. ascl–2307.
[44] Ahrens James, Geveci Berk, Law Charles, Hansen C, Johnson C. 36-Paraview: An end-user tool for large-data visualization. In: The visualization handbook. vol. 717, 2005, p. 717–31, 50038–1.
[45] Wilkinson Mark D, Dumontier Michel, Aalbersberg IJsbrand Jan, Appleton Gabrielle, Axton Myles, Baak Arie, Blomberg Niklas, Boiten Jan-Willem, da Silva Santos Luiz Bonino, Bourne Philip E, et al. The fair guiding principles for scientific data management and stewardship. Sci Data 2016;3(1):1–9.
[46] Taylor Brian. Tutorial-hertz contact stress. 2016.
[47] Plaza A, Carey GF. Local refinement of simplicial grids based on the skeleton. Appl Numer Math 2000;32:195–218.
[48] Wu Jian-Ying, Nguyen Vinh Phu. A length scale insensitive phase-field damage model for brittle fracture. J Mech Phys Solids 2018;119:20–42.
[49] Mandal Tushar Kanti, Nguyen Vinh Phu, Wu Jian-Ying. Length scale and mesh bias sensitivity of phase-field models for brittle and cohesive fracture. Eng Fract Mech 2019;217:106532.
[50] Gercek H. Poisson's ratio values for rocks. Int J Rock Mech Min Sci 2007;44(1):1–13.
[51] Mayo-Corrochano Cristina, Sánchez-Aparicio Luis Javier, Aira José-Ramón, Sanz-Arauz David, Moreno Esther, Melo Javier Pinilla. Assessment of the elastic properties of high-fired gypsum using the digital image correlation method. Constr Build Mater 2022;317:125945.
[52] Angela Mihai L, Goriely Alain. How to characterize a nonlinear elastic material? a review on nonlinear constitutive parameters in isotropic finite elasticity. Proc R Soc A 2017;473(2207):20170607.
[53] Goodman Richard E. Introduction to rock mechanics. John Wiley & Sons; 1991.
[54] Bhattacharyya Rudraprasad, Mahadevan Sankaran, Basu Prodyot K. Computationally efficient multiscale modeling for probabilistic analysis of cfrp composites with micro-scale spatial randomness. Compos Struct 2022;280:114884.
[55] Bhattacharyya Rudraprasad, Mahadevan Sankaran. Calibration and validation of multiscale model for ultimate strength prediction of composite laminates under uncertainty. ASCE-ASME J Risk Uncertain Eng Syst B 2021;8(2):021205.
[56] Wu Tao, Rosić B, Lorenzis Laura De, Matthies Hermann G. Parameter identification for phase-field modeling of fracture: a bayesian approach with sampling-free update. Comput Mech 2021;67:435–53.
[57] Bažant Zdeněk P, Vořechovskỳ Miroslav, Novák Drahomír. Asymptotic prediction of energetic-statistical size effect from deterministic finite-element solutions. J Eng Mech 2007;133(2):153–62.
[58] Grassl Peter, Bažant Zdeněk P. Random lattice-particle simulation of statistical size effect in quasi-brittle structures failing at crack initiation. J Eng Mech 2009;135(2):85–92.
[59] Navidtehrani Yousef, Betegón Covadonga, Martínez-Pañeda Emilio. A simple and robust abaqus implementation of the phase field fracture method. Appl Eng Sci 2021;6:100050.
[60] Sun Xiangming, Duddu Ravindra. A sequential non-iterative approach for modeling multi-ionic species reactive transport during localized corrosion. Finite Elem Anal Des 2019;166:103318.
[61] Sun Xiangming, Srinivasan Jayendran, Kelly Robert G, Duddu Ravindra. Numerical investigation of critical electrochemical factors for pitting corrosion using a multi-species reactive transport model. Corros. Sci. 2021;179:109130.